Noname manuscript No.
(will be inserted by the editor)

Tao Dai · Manuchehr Soleimani · Andy Adler

EIT Image Reconstruction with Four Dimensional Regularization

Received: date / Accepted: date

Abstract Electrical impedance tomography (EIT) reconstructs internal impedance images of the body from electrical measurements on body surface. The temporal resolution of EIT data can be very high, although the spatial resolution of the images is relatively low. Most EIT reconstruction algorithms calculate images from data frames independently, although data are actually highly correlated especially in high speed EIT systems. This paper proposes a 4-D EIT image reconstruction for functional EIT. The new approach is developed to directly use prior models of the temporal correlations among images and 3-D spatial correlations among image elements. A fast algorithm is also developed to reconstruct the regularized images. Image reconstruction is posed in terms of an augmented image and

Tao Dai

System and Computer Engineering, Carleton University, 1125 Colonel By Drive, Ottawa, Canada, K1S 5B6

E-mail: tdai@sce.carleton.ca

Manuchehr Soleimani

Electronic and Electrical Engineering, University of Bath, Bath, United Kingdom, BA2 7AY

E-mail: m.soleimani@bath.ac.uk

Andy Adler

System and Computer Engineering, Carleton University, 1125 Colonel By Drive, Ottawa, Canada, K1S 5B6

Tel.: (613) 520-2600 ext. 8785

Fax: (613) 520-5727

E-mail: adler@sce.carleton.ca

measurement vector which are concatenated from a specific number of previous and future frames. The reconstruction is then based on an augmented regularization matrix which reflects the *a priori* constraints on temporal and 3-D spatial correlations of image elements. A temporal factor reflecting the relative strength of the image correlation is objectively calculated from measurement data. Results show that image reconstruction models which account for inter-element correlations, in both space and time, show improved resolution and noise performance, in comparison to simpler image models.

Keywords Electrical Impedance Tomography · regularization · spatial and temporal priors · image reconstruction.

PACS 42.30.Wb · 87.63.Pn

Mathematics Subject Classification (2000) 92C55 · 65F22

1 Introduction

This paper develops a regularized image reconstruction formulation which directly accounts for temporal and spatial correlations between image elements in Electrical Impedance Tomography (EIT). EIT reconstructs images of the impedance distribution within the body from electrical measurement on the body surface. Because electrical current propagates diffusely in the body, EIT is a soft field tomography modality; moreover, EIT is ill-posed according to conditions of well-posed problems suggested by Hadamard. Thus, EIT reconstruction has poor spatial resolution and is very sensitive to data errors [22]. However, EIT can have excellent temporal resolution (frame rates as high as $1000/s$ have been achieved [31]) which makes EIT an attractive modality to monitor fast physiological activities which produce conductivity distribution changes. This is valuable for monitoring of cardiac [14,35], pulmonary [2,15,19] and brain [20] activities. The normal heart rate is physiologically limited to about 4 Hz, while a fibrillating heart rate can beat at up to 8 Hz [8]. The frequency content of images can be much higher than the heart rate as shown by the frequency content of the QRS complex which is mainly between 10–25 Hz [21]. For lung monitoring, high frequency ventilation (at frequencies of 5–25 Hz) is understood to be helpful to patients with respiratory distress; these patients have highly a non-uniform distribution of ventilation in the lung [16] and monitoring with EIT has been shown to

provide clinically useful information for control of ventilator settings [32]. Finally, EIT is potentially useful for monitoring brain activity. Tests such as visually evoked responses or monitoring for epilepsy result in rapid conductivity variations [29].

EIT uses single or multi-plane electrode arrangements to inject stimulation currents and measure the voltage response [13,23,17]. It is limited by the relatively small number of attached electrodes, and the severe ill-conditioning of the inverse problem due to the surface measurements and diffuse nature of electrical stimulation. In order to calculate a "reasonable" image, regularization techniques are required. Such regularized image reconstruction can be statistically formulated, in terms of *a priori* information, as a prior matrix describing image element values and the correlation between them. In many EIT algorithms, the zeroth order Tikhonov priors are commonly used [10,33]. While such priors are easy to compute, they assume that elements of the conductivity distributions are statistically independent – which is clearly not true for most EIT applications. Previously, shape-based inverse solutions were investigated in EIT applications. These methods modelled spatial priors according to geometrical knowledge of the target surface. e.g., boundary element method (BEM) based 3-D solution [6], and spline-based 2-D solution [30].

Another limitation to the quality of EIT images is signal noise. In cases where the physiological changes are slow with respect to the frame rate, time averaging of frames may be used to reduce noise by the square root of the number of averaged frames, given uncorrelated noise. However, if EIT data acquisition rate is comparable to the rate of change in the imaged processes, time averaging sacrifices the temporal resolution. Some other signal uncertainties also introduce image degradations, e.g., electrode-skin contact impedance drift which causes image distortion over time [9]. In these cases, each frame of EIT data is typically reconstructed independently of the others. However, it is clear that individual data frames are not completely independent, but do contain useful temporal correlations which could be exploited to improve EIT image noise performance and resolution.

Temporal image reconstruction can be represented as a linear tracking problem. In [25,26], *a priori* information about "temporal smoothness" was considered by adding one term which measures the variation between adjacent images, into the *Tikhonov-Phillips* minimization task. Another temporal

reconstruction method in EIT is the Kalman filter [34,27], in which the image at each instant is estimated from the current data and the previous image estimate.

In this paper, we make the novel contribution of a general approach to model the 4-D (temporal and 3-D spatial) correlations in the regularization prior. As image elements move further apart in space and time, the correlation between them is modelled to decrease exponentially, with exponential constants η and γ in space and time, respectively. This approach reconstructs each 3-D image at frame t using the set of data in frames $t-d$ to $t+d$, where d is the frame window width. Next, in order to reduce the computational burden of such large models, we develop an efficient formulation of the inverse matrices. This paper is an extension of our conference publication [12], where we considered only the vertical inter-slice correlation. In the results section, we show that such 4-D prior modelling gives improvements in both resolution and noise performance in the reconstructed images.

2 Methods

We consider an EIT system with n_E electrodes placed in 2 rings on body surface using planar placement [17] and adjacent current stimulation with parallel voltage measurement. n_E current stimulation patterns are sequentially applied and n_V differential measurements are made for each stimulation. We do not measure the voltages on the stimulation electrodes (however, given the proper hardware, such measurements are recommended [5]), thus $n_V = n_E - 3$ and the total number of measurements within one data frame is $n_M = n_E \times (n_E - 3)$. Difference EIT calculates difference signal $\mathbf{y} \in \mathbb{R}^{n_M}$, $\mathbf{y}_i = \mathbf{v}_i - [\mathbf{v}_0]_i$, or normalized as $\mathbf{y}_i = (\mathbf{v}_i - [\mathbf{v}_0]_i)/[\mathbf{v}_0]_i$, where the subscript i represents the measurement sequence. $[\mathbf{v}_0]_i$ is the reference measurement, obtained at a time when conductivity is more stable (such as diastole during a breath hold). In real applications, $\mathbf{v}_0$ can be obtained by averaging over several cycles of ventilation.

The body under investigation is modelled as a cylindrical finite element model (FEM) with n_N piecewise smooth tetrahedral elements, represented by a vector $\boldsymbol{\sigma} \in \mathbb{R}^{n_N}$ ($\boldsymbol{\sigma}$ represents conductivity in this paragraph, elsewhere in this paper, σ is the standard deviation). Difference EIT calculates a vector of conductivity change, $\mathbf{x}_i = \boldsymbol{\sigma}_i - [\boldsymbol{\sigma}_0]_i$ between the present conductivity distribution, $\boldsymbol{\sigma}$, and the reference conductivity distribution, $\boldsymbol{\sigma}_0$, which is typically assumed to be homogenous (in this paper, $\boldsymbol{\sigma}_0$

= 1S/m). For small variations around $\boldsymbol{\sigma}_0$, the relationship between the conductivity change image $\mathbf{x}_t$ and difference measurements $\mathbf{y}_t$ at time t can be linearized (giving the difference EIT forward model):

$$\mathbf{y}_t = \mathbf{J}\mathbf{x}_t + \mathbf{n} \tag{1}$$

where $\mathbf{J} \in \mathbb{R}^{n_M \times n_N}$ is the Jacobian or sensitivity matrix; $\mathbf{n} \in \mathbb{R}^{n_M}$ is the measurement noise which is assumed to be uncorrelated white Gaussian. $\mathbf{J}$ is calculated from the FEM as $\mathbf{J}_{ij} = \frac{\partial \mathbf{y}_i}{\partial \mathbf{x}_j}\Big|_{\boldsymbol{\sigma}_0}$. The goal of regularized image reconstruction (such as [10,3]) is to calculate a conductivity change estimate, $\hat{\mathbf{x}}_t$, which is both faithful to the measurements, $\mathbf{y}_t$, and to *a priori* constraints on a "reasonable" image.

In subsequent sections we develop a formulation for the spatial and temporal *a priori* image element correlations, and use these to consider the following reconstruction approaches: 1) *Gauss-Newton (GN) inverse*, using the current measurement frame $\mathbf{y}_t$ only; 2) *Temporal inverse*, using measurement frames $\mathbf{y}_{t-d} \ \cdots \ \mathbf{y}_{t+d}$ based on a temporal prior model; 3) *3-D spatial inverse*, using measurement $\mathbf{y}_t$ based on a 3-D spatial prior model with spatial correlations among elements; and 4) *4-D prior inverse*, using measurement $\mathbf{y}_{t-d} \ \cdots \ \mathbf{y}_{t+d}$ and a temporal and and 3-D spatial model.

2.1 One-step linear Gauss-Newton solver

Regularized image reconstruction for EIT based on the one-step linearized Gauss-Newton (GN) solver was first introduced into EIT by [36], and has been widely used. It calculates a linear reconstruction matrix which may subsequently be used be used for rapid imaging, and allows taking advantage of sophisticated regularization modalities to solve the inverse problem. This method seeks a solution, $\hat{\mathbf{x}}$, which minimizes the error in the form

$$\|\mathbf{y} - \mathbf{J}\hat{\mathbf{x}}\|^2_{\boldsymbol{\Sigma}_n^{-1}} + \|\hat{\mathbf{x}} - \mathbf{x}^\circ\|^2_{\boldsymbol{\Sigma}_x^{-1}} \tag{2}$$

here $\mathbf{x}^\circ$ is the expected value of element conductivity changes, which is zero for difference EIT since it assumes that the conductivity changes may be equally positive or negative. $\boldsymbol{\Sigma}_n \in \mathbb{R}^{n_M \times n_M}$ is the covariance matrix of the measurement noise $\mathbf{n}$. Since $\mathbf{n}$ is uncorrelated, $\boldsymbol{\Sigma}_n$ is a diagonal matrix with $[\boldsymbol{\Sigma}_n]_{i,i} = \sigma_i^2$, where σ_i^2 is the noise variance at measurement i. $\boldsymbol{\Sigma}_x \in \mathbb{R}^{n_N \times n_N}$ is the covariance matrix of the expected image, which we consider in detail subsequently.

Instead of calculating $\mathbf{\Sigma}_n$ and $\mathbf{\Sigma}_x$ directly, most proposed approaches have developed models of the inverse of these matrices heuristically. We use the following terminology: $\mathbf{W} = \sigma_n^2 \mathbf{\Sigma}_n^{-1}$ and $\mathbf{R} = \sigma_x^2 \mathbf{\Sigma}_x^{-1}$, where σ_n is the average measurement noise amplitude and σ_x is the *a priori* amplitude of conductivity changes. $\mathbf{W}$ models the relative measurement accuracy across channels. For uncorrelated noise, each diagonal element is proportional to the signal-to-noise-ratio (SNR). For difference EIT with identical channels, $\mathbf{W}$ is an identity matrix; this paper uses model, $\mathbf{W} = \mathbf{I}$. The regularization matrix $\mathbf{R}$ may be understood to model the "unlikelihood" of image element configurations. A simple model for $\mathbf{R}$ may consider all configurations equally likely, while more sophisticated models, such as the ones we develop, may consider smooth distributions more likely than rapidly changing ones.

By solving (2) and defining the hyperparameter $\lambda = \sigma_n / \sigma_x$, a linearized, one-step inverse solution is obtained

$$\hat{\mathbf{x}} = \left(\mathbf{J}^T \mathbf{W} \mathbf{J} + \lambda^2 \mathbf{R} \right)^{-1} \mathbf{J}^T \mathbf{W} \mathbf{y} = \mathbf{B} \mathbf{y} \tag{3}$$

where $\mathbf{B} = \left(\mathbf{J}^T \mathbf{W} \mathbf{J} + \lambda^2 \mathbf{R} \right)^{-1} \mathbf{J}^T \mathbf{W}$ is the linear, one-step reconstruction matrix. λ controls the trade-off between resolution and noise attenuation in the reconstructed image.

By assuming that image elements are independent to each other and have identical expected magnitude, $\mathbf{R}$ becomes an identity matrix $\mathbf{I}$ and (3) uses zeroth-order Tikhonov regularization. For EIT, since the measured data is much more sensitive to boundary elements than elements deep inside, such solutions tend to push reconstructed noise toward the boundary. In order to compensate the sensitivity discrepancy, $\mathbf{R}$ may be scaled with the sensitivity of each element, so that $\mathbf{R}$ is a diagonal matrix with elements $[\mathbf{R}]_{i,i} = \left[\mathbf{J}^T \mathbf{J} \right]_{i,i}^p$. This is the NOSER prior of [10] for an exponent p. One similar variance compensation strategy was proposed as *variance uniformization* in [7].

In (3), the term to be inverted is of size $n_N \times n_N$. This is especially cumbersome in 3D (and 4D) reconstruction models, where n_N may be on the order of ten or a hundred thousand. This calculation is then very demanding on computer time and memory. We address this issue by rewriting the matrix $\mathbf{B}$ using the *data form* (also referred to as the Wiener filter form) [4] as:

$$\mathbf{B} = \mathbf{P} \mathbf{J}^T \left(\mathbf{J} \mathbf{P} \mathbf{J}^T + \lambda^2 \mathbf{V} \right)^{-1} \tag{4}$$

where $\mathbf{P} = \mathbf{R}^{-1} = \mathbf{\Sigma}_x/\sigma_x^2$ and $\mathbf{V} = \mathbf{W}^{-1} = \mathbf{\Sigma}_n/\sigma_n^2$; Using (4), the size of the inverted matrix is significantly reduced to $n_M \times n_M$. This is especially helpful for large scale models, such as 3-D EIT models and the temporal inverse be introduced below.

2.2 Temporal solver

In this section, we develop a temporal image reconstruction algorithm which calculates the image at a current frame using a set of data frames nearby in time. This approach differs from Kalman filter based algorithms [34] which estimate image $\mathbf{x}_t$ based on measurements $\mathbf{y}_t$ and the previous image estimate $\mathbf{x}_{t-1}$. The *temporal solver* treats the estimate of the image frame sequence as a single inverse problem, with a regularization prior which accounts for both spatial and temporal correlations between image elements.

2.2.1 Temporal reconstruction

The temporal solver considers a sequence of $2d+1$ measurements frames from $t-d$ to $t+d$ around the current frame, t. Given a vertically concatenated sequence of measurements frames $\tilde{\mathbf{y}}_t$ and the corresponding concatenated images $\tilde{\mathbf{x}}_t$,

$$\begin{aligned} \tilde{\mathbf{y}}_t &= [\mathbf{y}_{t-d}^T \ \cdots \ \mathbf{y}_t^T \ \cdots \ \mathbf{y}_{t+d}^T]^T \\ \tilde{\mathbf{x}}_t &= [\mathbf{x}_{t-d}^T \ \cdots \ \mathbf{x}_t^T \ \cdots \ \mathbf{x}_{t+d}^T]^T \end{aligned} \tag{5}$$

the direct temporal forward model (1) is rewritten as

$$\tilde{\mathbf{y}}_t = \tilde{\mathbf{J}}\tilde{\mathbf{x}}_t + \tilde{\mathbf{n}} \tag{6}$$

where $\tilde{\mathbf{n}} = [\mathbf{n}_{t-d}^T \ \cdots \ \mathbf{n}_t^T \ \cdots \ \mathbf{n}_d^T]^T$. We consider that the model structure is constant, and thus $\mathbf{J}$ does not vary with time, giving $\tilde{\mathbf{J}} = \mathbf{I} \otimes \mathbf{J}$, where the identity matrix $\mathbf{I}$ has size $2d+1$, and $\otimes$ is the Kronecker product.

The relationship between corresponding image elements between adjacent frames can be represented by an inter-frame correlation which has a value between 0 (independent) and 1 (fully dependent). The correlation could possibly be negative if subsequent frames have inverse correlation, although this

scenario is physiologically unrealistic. As frames become separated in time, the inter-frame correlation decreases; for a frame separation of δ, the inter-frame correlation is $exp(-|\delta|/\gamma)$, where γ is the temporal exponential decay factor in units of frames. Frames with large time difference, $|\delta| > d$, are considered independent. The one-step inverse (4) for image reconstruction then becomes

$$\tilde{\mathbf{B}} = \tilde{\mathbf{P}}\tilde{\mathbf{J}}^T \left(\tilde{\mathbf{J}}\tilde{\mathbf{P}}\tilde{\mathbf{J}}^T + \lambda^2\tilde{\mathbf{V}}\right)^{-1} \tag{7}$$

where $\tilde{\mathbf{V}} = \mathbf{I} \otimes \mathbf{V}$. $\tilde{\mathbf{V}}$ is diagonal since measurement noise is uncorrelated between frames. $\tilde{\mathbf{P}} = \mathbf{\Gamma} \otimes \mathbf{P}$, where $\mathbf{\Gamma}$ is the temporal weight matrix of an image sequence $\tilde{\mathbf{x}}$ and is defined to have the form as

$$[\mathbf{\Gamma}]_{i,j} = exp(-\frac{|i-j|}{\gamma}) \quad i,j = -d \ \ldots \ d. \tag{8}$$

From (7) and (8),

$$\tilde{\mathbf{B}} = \left[\mathbf{\Gamma} \otimes \left(\mathbf{P}\mathbf{J}^T\right)\right] \left[\mathbf{\Gamma} \otimes \left(\mathbf{J}\mathbf{P}\mathbf{J}^T\right) + \lambda^2 \left(\mathbf{I} \otimes \mathbf{V}\right)\right]^{-1} \tag{9}$$

Given $\tilde{\mathbf{B}}$, the one step solution for the current image ($\hat{\mathbf{x}}_t$) is rewritten as

$$\hat{\mathbf{x}}_t = \tilde{\mathbf{B}}_0 \tilde{\mathbf{y}}_t \tag{10}$$

where $\tilde{\mathbf{B}}_0$ is the rows $n_M \times d + 1 \ \ldots \ n_M \times (d+1)$ of $\tilde{\mathbf{B}}$.

2.2.2 Parameter selection

The γ is a hyperparameter of the system; it depends on the data acquisition frame rate, the speed of underlying conductivity changes and the system noise level. This section develops an approach to estimate the value of γ from the measurement sequence. By taking covariance on both sides of (6), we have the estimated covariance matrix of the data as

$$\hat{\mathbf{\Sigma}}_{\tilde{\mathbf{y}}} = \tilde{\mathbf{J}}\mathbf{\Sigma}_{\tilde{\mathbf{x}}}\tilde{\mathbf{J}}^t + \mathbf{\Sigma}_{\tilde{\mathbf{n}}} \tag{11}$$

the optimal γ is chosen so that the error between the true data covariance matrix $\mathbf{\Sigma}_{\tilde{\mathbf{y}}}$ and the estimated one $\hat{\mathbf{\Sigma}}_{\tilde{\mathbf{y}}}$ is minimized as

$$\gamma = \arg\min_{\gamma} \left\| \mathbf{\Sigma}_{\tilde{\mathbf{y}}} - \mathbf{\Sigma}_{\tilde{\mathbf{n}}} - \tilde{\mathbf{J}}\mathbf{\Sigma}_{\tilde{\mathbf{x}}}\tilde{\mathbf{J}}^t \right\|_F^2 \tag{12}$$

where the subscript F is the *Frobenius norm*. Since $\mathbf{\Sigma}_{\tilde{\mathbf{x}}} = \mathbf{\Gamma} \otimes \mathbf{\Sigma}_{\mathbf{X}}$ and $\tilde{\mathbf{J}} = \mathbf{I} \otimes \mathbf{J}$, (12) becomes

$$\gamma = \arg\min_{\gamma} \left\| \mathbf{\Sigma}_{\tilde{\mathbf{y}}} - \mathbf{\Sigma}_{\tilde{\mathbf{n}}} - \mathbf{\Gamma} \otimes \left(\mathbf{J}\mathbf{\Sigma}_{\mathbf{X}}\mathbf{J}^t\right) \right\|_F^2 \tag{13}$$

By taking covariance on both sides of (1), we have

$$\mathbf{\Sigma_y} = \mathbf{J}\mathbf{\Sigma_x}\mathbf{J}^t + \mathbf{\Sigma_n} \tag{14}$$

so that $\mathbf{J}\mathbf{\Sigma_x}\mathbf{J}^t = \mathbf{\Sigma_y} - \mathbf{\Sigma_n}$; we also have $\mathbf{\Sigma_{\tilde{n}}} = \mathbf{I} \otimes \mathbf{\Sigma_n}$ and $\mathbf{\Sigma_{\tilde{y}}} = \mathbf{\Gamma_y} \otimes \mathbf{\Sigma_y}$, where $\mathbf{\Gamma_y} \in \mathbb{R}^{(2d+1)\times(2d+1)}$ is the correlation matrix of $\tilde{\mathbf{y}}$. Thus the optimal γ is calculated by

$$\gamma = \arg\min_{\gamma} \left\| \mathbf{\Gamma_y} \otimes \mathbf{\Sigma_y} - \mathbf{I} \otimes \mathbf{\Sigma_n} - \mathbf{\Gamma} \otimes \left(\mathbf{\Sigma_y} - \mathbf{\Sigma_n} \right) \right\|_F^2 \tag{15}$$

$\mathbf{\Gamma_y}$ and $\mathbf{\Sigma_y}$ can be calculated directly from the data. $\mathbf{\Sigma_n}$ can be measured by calibration of EIT system. For computational efficiency, (15) can be simplified as

$$\gamma = \arg\min_{\gamma} \left\| \mathbf{\Gamma_y} \left\| \mathbf{\Sigma_y} \right\|_F^2 - \mathbf{I} \left\| \mathbf{\Sigma_n} \right\|_F^2 - \mathbf{\Gamma} \left\| \mathbf{\Sigma_y} - \mathbf{\Sigma_n} \right\|_F^2 \right\|_F^2 \tag{16}$$

where $\mathbf{\Gamma_y}$, $\left\| \mathbf{\Sigma_y} \right\|_F^2$, $\left\| \mathbf{\Sigma_n} \right\|_F^2$ and $\left\| \mathbf{\Sigma_y} - \mathbf{\Sigma_n} \right\|_F^2$ may be precalculated. Since $\mathbf{\Gamma}$ is relatively small ($\mathbb{R}^{(2d+1)\times(2d+1)}$) this optimization is performed directly by bisection search between limits.

2.3 3-D spatial prior with full model correlation

The most common assumption for image prior models is to consider independent image elements; examples are the zeroth order Tikohonov prior [36], and the NOSER prior [10]. When elements are independent, the inter-element correlation is zero, meaning $\mathbf{\Sigma}_x$ is diagonal. Another common assumption is to consider that elements are locally correlated [33]. In this case $\mathbf{\Sigma}_x$ has a sparse non-diagonal structure since in the z direction only adjacent elements are considered correlated. We consider that these approaches have two important limitations. First, they do not reflect adequately the scale of the correlations in the images; image elements are correlated globally. Secondly, the spatial frequency behaviour will depend on the size of the image elements, with a larger spatial correlation being imposed for larger elements. Thus, a fine and coarse model with the same spatial prior do not really implement the same prior model, and the prior model will be spatially non-uniform for a model with localized mesh refinement.

In this section, we develop a 3-D spatial prior model which accounts for the full correlation model. It is more computationally expensive to compute than simpler prior models, but this is only performed as a precalculation, not during image reconstruction. This model is based on three factors: 1) a sensitivity

weighting, where elements are weighted by the norm of the measurement sensitivity, 2) exponentially decreasing spatial correlation with inter-element distance, and 3) an additional smoothness constraint for elements in regions with poor sensitivity, such as above and below the electrode planes.

2.3.1 Sensitivity weighting

The sensitivity of measurements to a change in element i is the norm of the ith column of the Jacobian, $\|\mathbf{J}_{:,i}\| = [\mathbf{J}^T\mathbf{J}]_{i,i}$. As mentioned, we consider this weighting to be too strong for high sensitivity elements, and tends to push image artefacts toward the center where the sensitivity is much lower. Instead, we use a sensitivity weighting of $p = 0.5$. The choice of p is a heuristic compromise between the pushing noise to the boundary ($p = 0$) or to the centre ($p = 1$).

The inter-element sensitivity is based on the product of the square root of the sensitivity to each element. Thus, we define the sensitivity weighting part of the prior matrix $\mathbf{P}_N^{\frac{1}{2}}$ as

$$\left[\mathbf{P}_N^{\frac{1}{2}}\right]_{i,i} = \left[\mathbf{J}^T\mathbf{J}\right]_{i,i}^{-\frac{p}{2}} \tag{17}$$

Based on (17) the 3-D spatial prior is defined as

$$\mathbf{P} = \mathbf{P}_N^{\frac{1}{2}}\mathbf{P}_C\mathbf{P}_N^{\frac{1}{2}} \tag{18}$$

where $\mathbf{P}_C$ is the spatial correlation matrix

2.3.2 Exponential spatial correlations

Given two small image elements i, j, centred at $\mathbf{r}_i = (x_i, y_i, z_i)$ and $\mathbf{r}_j = (x_j, y_j, z_j)$, the spatial correlation is defined in terms of a spatial exponential constant η in units of distance. Elements closer together than η are highly correlated, and those further apart have low correlation. Thus

$$[\mathbf{P}_C]_{i,j} = exp(-\frac{\|\mathbf{r}_i - \mathbf{r}_j\|}{\eta}) \tag{19}$$

However, for larger finite elements, (19) has to be modified because not all parts of each image element are at distance $\|\mathbf{r}_i - \mathbf{r}_j\|$ from each other. Instead we replace it with

$$[\mathbf{P}_C]_{i,j} = \frac{1}{V_iV_j}\int_{E_i}\int_{E_j} exp(-\frac{\|\mathbf{r}_i - \mathbf{r}_j\|}{\eta})d\mathbf{r}_j d\mathbf{r}_i \tag{20}$$

where the integrals are over the volume of finite elements E_i and E_j. V_i and V_j are the volumes of each element, where $V_i = \int_{E_i} d\mathbf{r}_i$. We derive a closed form estimate for the integrals in (20) below.

2.3.3 Low sensitivity constraint

The EIT sensitivity is extremely low for regions above and below the electrode bands. This has important consequences for image reconstruction because it further increases the ill-conditioning of the EIT inverse. The consequence is that the algorithm may "push" image artefacts to these regions; since the measurement norm from these regions is so small, large artefacts have only a small effect on the data fit. To avoid this effect, it is possible to tightly crop the 3D FEM model near the electrode planes, but this also introduces artefacts, since it prevents the model current from flowing into these areas.

Using the exponential spatial correlations, it is possible to naturally account for low sensitivity regions by imposing a strong smoothness constraint. By dramatically increasing η for image elements in these regions, we force the algorithm to consider elements to be highly correlated, and reduce the effective degrees of freedom (or number of fitted parameters) allocated to this region. This has the advantage that it will reduce high spatial frequency artefacts, but does not arbitrarily and unnaturally impose a penalty on reconstructed image amplitude in these regions. Thus we modify (20),

$$[\mathbf{P}_C]_{i,j} = \frac{1}{V_i V_j} \int_{E_i} \int_{E_j} exp(-\frac{\|\mathbf{r}_i - \mathbf{r}_j\|}{\eta(\mathbf{r}_i, \mathbf{r}_j)}) d\mathbf{r}_j d\mathbf{r}_i \tag{21}$$

$$\text{where } \eta(\mathbf{r}_i, \mathbf{r}_j) = \begin{cases} \eta_0 & \text{if } z_{p1} \le z_i \le z_{p2} \text{ or } z_{p1} \le z_j \le z_{p2} \\ K(z_i, z_j)\eta_0 & \text{otherwise.} \end{cases}$$

where η_0 is the value used in the central regional, z_{p1} and z_{p2} are the vertical positions of the electrode planes, and $K(z_i, z_j)$ is a penalty term which may depend on the distance from the z_{p1} and z_{p2}. For simplicity, we use a constant value of $K = 5$ in this paper. Note that the low sensitivity penalty is only imposed if both z_i and z_j are outside the electrode plane.

2.3.4 Integral of exponential correlations

The integrals in (20) are over the coordinates of each finite element simplex. In order to develop a closed form integral we model each element instead as a sphere of the same volume and centre coordinates as the original finite element simplex. For a simplex of coordinates $(x_k, y_k, z_k), k = 1 \dots 4$, we have volume $V = \frac{1}{3!} detD$, where the kth row of $D_{k,:} = [1, x_k, y_k, z_k]$. From this volume, the sphere radius is $r = \sqrt[3]{\frac{3V}{4\pi}}$. With this model, the integral may be approximated as a 1-D integral over the line from $\mathbf{r}_i$

to $\mathbf{r}_j$. Based on element centres, ($\mathbf{r}_i$, $\mathbf{r}_j$) and radii (r_i, r_j), we calculate the (i,j) element of the 3-D spatial prior $\mathbf{P}_C$ as follows:

$$[\mathbf{P}_C]_{i,j} = \frac{1}{V_i V_j} \int_{-r_i}^{r_i} \int_{-r_j}^{r_j} exp(-\frac{|\Delta_{ij} + x + y|}{\eta}) dy dx \tag{22}$$

where $V_i = 2r_i$, $V_j = 2r_j$ and $\Delta_{ij} = \|\mathbf{r}_i - \mathbf{r}_j\|$.

Because of the absolute value, the inner integral has two cases:

$$\int_{-r_j}^{r_j} e^{-\frac{1}{\eta}|\Delta_{ij}+x+y|} dy = \eta e^{\frac{\Delta_{ij}+x}{\eta}} [e^{\frac{y}{\eta}}]_{-r_j}^{y'} - \eta e^{-\frac{\Delta_{ij}+x}{\eta}} [e^{-\frac{y}{\eta}}]_{y'}^{r_j} \tag{23}$$

where $y' = -(\Delta_{ij} + x)$ if $-r_j \leq \Delta_{ij} + x \leq r_j$ and is otherwise limited to the range $y' = \pm r_j$. Based on these cases, the outer integral is split into three portions $-r_i \leq x \leq x'$, $x' < x < x''$, and $x'' < x < r_i$, where $x' = min(r_i, -\Delta_{ij} - r_j)$ and $x'' = min(r_i, -\Delta_{ij} + r_j)$. Thus

$$\begin{aligned}
[\mathbf{P}_C]_{i,j} &= \frac{\eta}{4 r_i r_j} \left(\int_{-r_i}^{x'} e^{\frac{\Delta_{ij}+x}{\eta}} [e^{\frac{y}{\eta}}]_{-r_j}^{r_j} dx + \int_{-x''}^{r_i} e^{-\frac{\Delta_{ij}+x}{\eta}} [e^{\frac{y}{\eta}}]_{-r_j}^{r_j} dx \right. \\
&\left. + \int_{-x'}^{x''} e^{\frac{\Delta_{ij}+x}{\eta}} [e^{\frac{y}{\eta}}]_{-r_j}^{-(\Delta_{i,j}+x)} + e^{-\frac{\Delta_{ij}+x}{\eta}} [e^{\frac{y}{\eta}}]_{-r_j}^{(\Delta_{i,j}+x)} dx \right) \\
&= \frac{\eta^2}{4 r_i r_j} \left(e^{-\frac{\Delta_{ij}}{\eta}} \left[e^{\frac{x}{\eta}} \right]_{-r_i - x''}^{+r_i + x'} \left[e^{\frac{y}{\eta}} \right]_{-r_j}^{+r_j} + \left[\frac{2}{\eta} x - e^{-\frac{\Delta_{i,j} + r_j - x}{\eta}} + e^{-\frac{\Delta_{i,j} - r_j + x}{\eta}} \right]_{x'}^{x''} \right)
\end{aligned} \tag{24}$$

2.4 Methods: Simulations

Numerical simulations were designed to model the movement of blood through the mitral valve during systolic ejection. We use the following average values for healthy humans: Mitral valve area is 7.1 ± 1.3 cm^2 [24] and the rate of change of left ventricular volume is 473 ml/s [18]. These values correspond to a mitral radius of 1.5 cm; we thus simulate the ventricular ejection blood flow as conductive sphere of 1.5 cm radius moving at 97.8 cm/s.

Numerical simulations were conducted using a 3-D cylindrical FEM model with 77999 elements using the Netgen 4.4 software. Illustrated as Fig. (1), the model height is 30 cm ($z : 0 \sim 30$); two electrode rings (8 electrodes each) were attached at heights $z = 10,\ 20$ cm using adjacent stimulation and measurement pattern. The systolic ejection is upwards and lateral which can be roughly simulated as a helical pattern movement in blood vessel. Illustrated as Fig. (2), inside the model, a conductive sphere with radius 1.5 cm rotates and rises in a the helical pattern at a uniform speed from $z = 7.5$ cm to

$z = 22.5$ cm, moving clockwise (bird's eye view) along a trajectory with radius 10 cm. The background material was set to a homogeneous conductivity, $\boldsymbol{\sigma}_0 = 1.0$ S/m, and the spherical target to be more conductive: $\boldsymbol{\sigma} = 1.2$ S/m. The projection of the movement trajectory on the $x-y$ plane is a full circle, and corresponds to a movement of 64.5 cm. Thus, to model systolic ejection, one cycle of conductive sphere movement is set to be 0.66 seconds. In model an EIT system with a frame rate ≈ 40 frames/s, and thus simulate a movement rate of the conductive sphere of 26 frames/cycle.

The noise performance of the algorithms was tested by adding pseudo random, zero mean Gaussian noise to each image reconstruction (with the same random seed). Images were reconstructed on a 3-D model generated by using the *EIDORS* software [3] with 10 vertical slices and 256 elements on each slice; this inverse model differs from the simulation model to avoid the inverse crime[11].

3 Results

Reconstructed targets were calculated using *EIDORS* to evaluate four algorithms with different regularization priors: 1) *GN solver*, with no spatial or temporal prior model; 2) *temporal solver*, with a temporal but no spatial prior model; 3) *3-D prior solver*, with a spatial but no temporal prior model; and 4) *4-D prior solver*, with both a spatial and temporal prior model. The measurement to be reconstructed was chosen for the conductive sphere in a left anterior position, and slightly closer to the bottom than the top electrode plane. Fig 2 shows the conductive sphere location $(x, y, z) = (3.1, -9.5, 14.25)$ and that of the position of the sphere during the $d = 3$ frames before and after the centre measurement used in the image reconstruction. The reconstructions were plotted as nine vertical slices chosen from $z = 9$ cm to $z = 21$ cm. Figures 3 and 4 show images with Noise to Signal Ratios (NSR) of 0 and 2, respectively. NSR was defined as $\sigma_{\mathbf{n}}/\bar{\mathbf{y}}$, where $\bar{\mathbf{y}}$ is the mean value of the difference signal. The optimal value of γ was calculated based on Section 2.2 as 0.97 and 0.89 frames, for NSR=0 and NSR= 2, respectively. Different random seeds were used without evidently different results observed. The value of η was chosen to be 3 cm or 0.1 of the medium diameter. This value will tend to penalize spatial frequency content in images that is less than 10% of the diameter, or 1% of the area. This value (1%) corresponds approximately the number of independent measurements available from this EIT system (104).

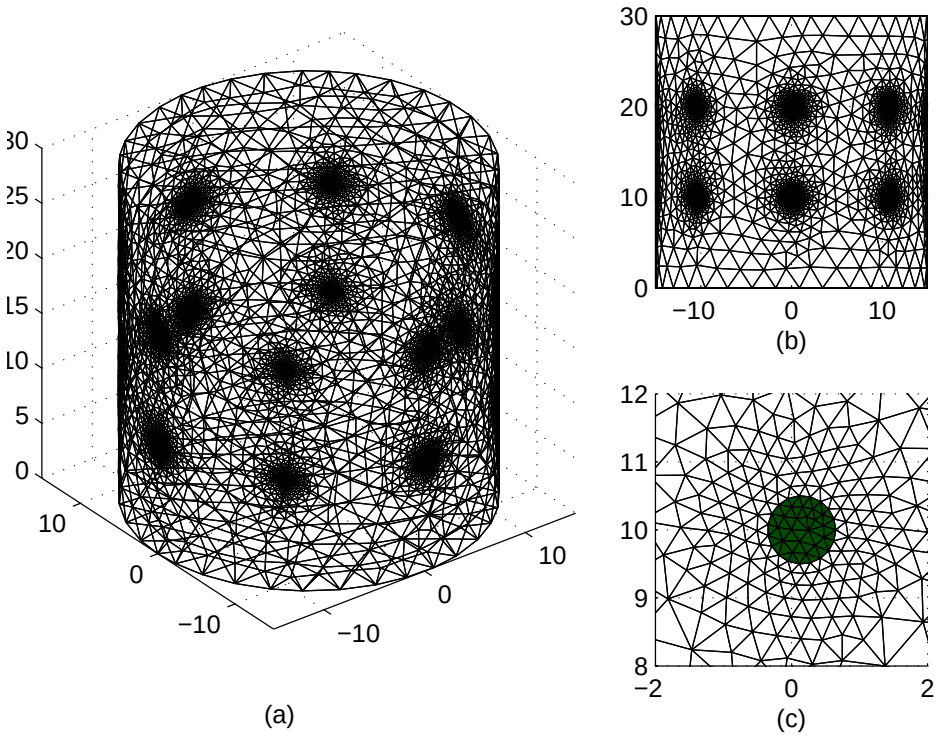

Fig. 1 The forward model: 3-D cylindrical finite element model generated from netgen. The tank of height 30 cm and diameter 30 cm is meshed with 77999 tetrahedral elements. Sixteen circular electrodes (diameter 1.0 cm) are placed in two planes (8 electrodes each) located at $z = 10$ cm and 20 cm, respectively. Mesh refinement is applied around electrodes. (a) 3-D forward model; (b) side view, (c) one of electrodes with mesh refined around it.

In order to allow comparison across algorithms, we select identical hyperparameter for all algorithms tested. When λ is low, there is no significant difference between the GN method and temporal/3-D/4-D priors methods. We empirically choose a relatively large value of $\lambda = 0.5$ to illustrate the effect in higher noise conditions. Figures 3 and 4 show reconstructed images for each algorithm with no noise and with a fairly large (NSR=2) level of noise. All images show reconstructions in arbitrary units and are scaled equally.

In order to evaluate the quality of reconstructed images, the following figures of merit are used: 1) *target resolution*: the point spread function (PSF) of the target is small in the horizontal plane, and the off plane ghosts (which illustrated as virtual targets in the planes other than the target plane $z = 14.25$) are small; 2) *reconstruction position error*: the planar position of the reconstructed target is correct. The

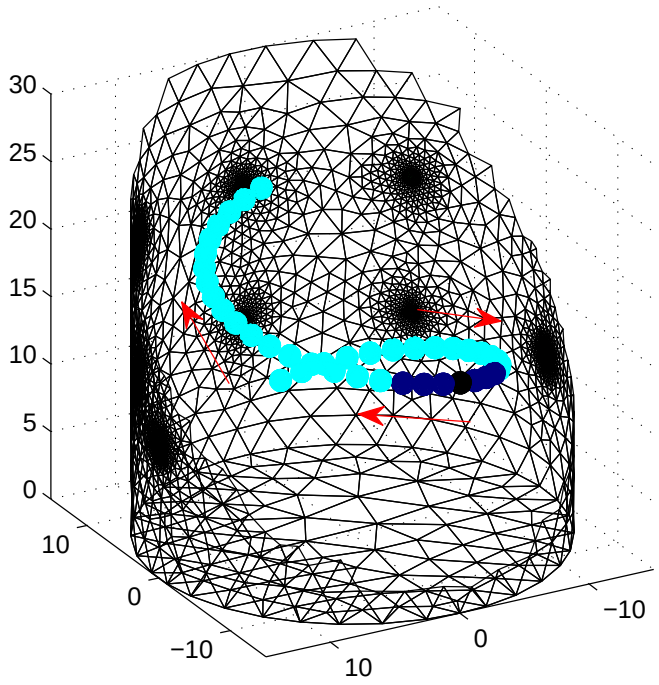

Fig. 2 The trajectory of a spherical conductive target of radius 1.5 cm, representing the bolus left ventricular ejection. To clarify the target movement, the tank model is cropped by the plane defined by $y + 15 < z$. The target ($(x, y, z) = (3.1, -9.5, 14.25)$) is black in the position at which the frame is taken for image reconstruction. Targets in dark blue are positions on from which data frames are measured and used in the calculation by the temporal solver ($d = 3$ as illustrated).

planar position of the reconstructed target is calculated from the slice at $z = 14.25$ using the position definition described in [1]: the centre of gravity is computed on a zone defined by half magnitude of image; and 3) *noise performance*: the reconstructed images should be robust to measurement noise. Based on these criteria and Figs. 3, 4 and Table 1, we observe that: 1) *target resolution*: 4-D prior solver is ranked as the highest resolution; 2) *reconstruction position error*: The position error (distance to the optimal position $(3.1, -9.5)$) is listed as Table 1. 4-D prior solver achieves best planar position accuracy for both the noisy and noise-free situations; 3) *noise performance*: temporal prior solver has the best noise robustness. However, 3-D prior solver introduces more artefacts when noise is added.

Figure (5) shows the relationship of the hyperparameter γ to the noise and speed of conductivity change. γ is a measure of the exponential rate of loss of coherence between images elements across

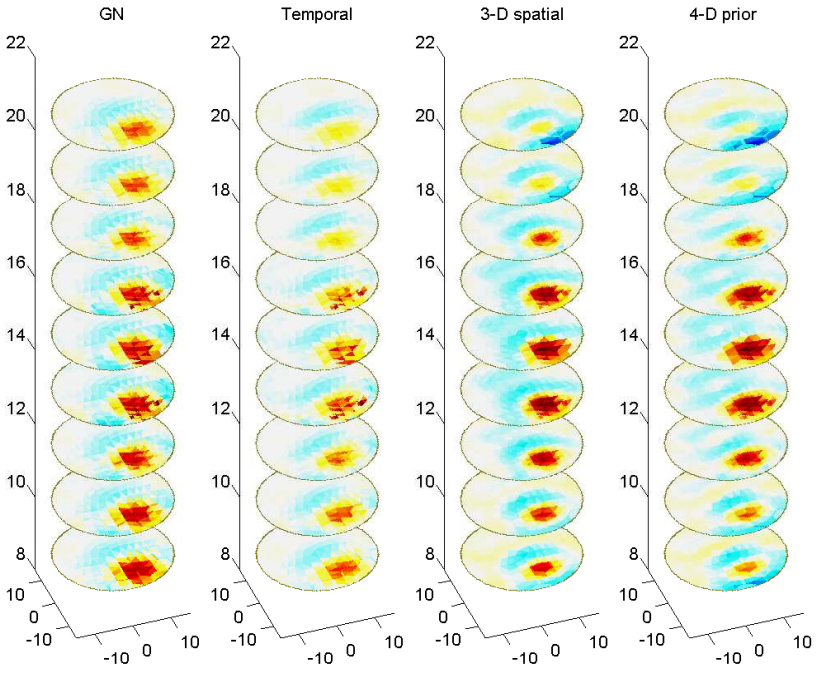

Fig. 3 Comparison of algorithm images with no noise. From right to left, algorithms are: conventional GN solver, temporal solver, 3-D prior solver, and 4-D prior solver. The image to be reconstructed was at $t = 0.3$ sec. Electrode planes were at $z = 10$ and 20 cm. Parameters are NSR=0, $\lambda = 0.5$, $\eta = 0.1$, $\gamma = 32.8$.

Table 1 The list of planar positions of reconstructed target at the level $z = 14.25$, and the distances to the optimal position $(3.1, -9.5)$.

solvers	$NSR = 0$		$NSR = 2$	
	(x,y) (cm)	distance (cm)	(x,y) (cm)	distance (cm)
Conventional GN	(4.15,-9.93)	1.14	(3.93,-9.83)	0.89
Temporal prior solver	(3.93,-9.97)	0.95	(3.84,-9.98)	0.88
3-D prior solver	(3.91,-9.51)	0.81	(3.95,-9.05)	0.96
4-D prior solver	(3.76 -9.04)	0.80	(3.63,-8.84)	0.85

frames. The figure shows, as expected, that γ decreases as the conductivity change rate increases (or, equivalently, as the data frame rate decreases) or as the noise level increases. At very low system speed and/or very high NSR, γ reaches zero, indicating that adjacent frames are independent, and the temporal prior provides no advantage.

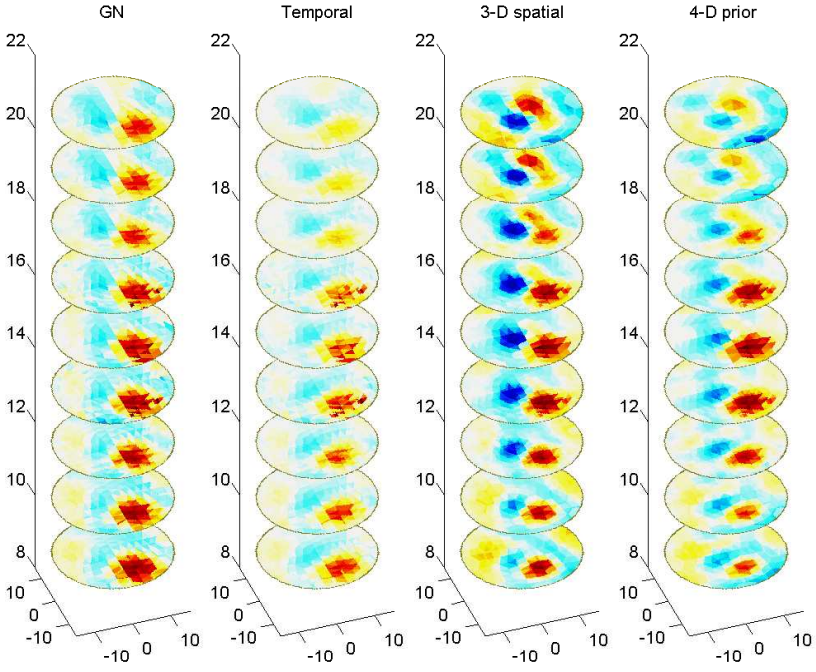

Fig. 4 Comparison of algorithm images with noise. From right to left, algorithms are: conventional GN solver, temporal solver, 3-D prior solver, and 4-D prior solver. The image to be reconstructed was at $t = 0.3$ sec. Electrode planes were at $z = 10$ and 20 cm. Algorithm parameters are NSR=2, $\lambda = 0.5$, $\eta = 0.1$, $\gamma = 8.6$.

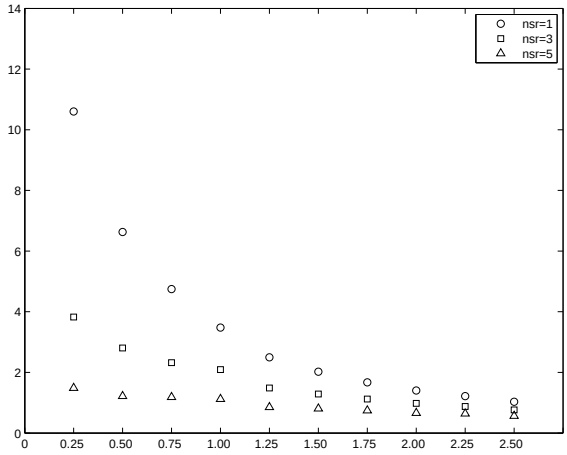

Fig. 5 The inter-frame correlation γ as a function of target speed and noise level. *vertical axis* temporal exponential decay parameter γ (units frames) calculated from measurements. *horizontal axis* target frame period relative to the frame rate of 40 frame/s used elsewhere. Image reconstruction used $d = 3$,$\lambda = 0.5$.

4 Discussion

Traditionally, EIT reconstruction algorithms assume each data frame to be independent. However, since EIT is able to make measurements at high frame rates, we know *a priori* that image frames are correlated. Intuitively, it makes sense that a sophisticated image reconstruction algorithm should be able to take advantage of known correlations in the input data to benefit the reconstructed images.

Kalman filter techniques in EIT (such as [34]) provide a temporal image reconstruction based on iterative tracking. The estimated image is calculated from the current data and the previous image estimate. This differs from our proposed method which calculates a single step solution using a "frame window" with d frames before and after the current frame. It improves over Kalman filter based algorithms by allowing an explicit control over the regularization prior and the weighting of measured data. The one-step temporal reconstruction method was applied to experimental data from the Magnetic Inductance Tomography (MIT) which is a similar inverse problem case to EIT [28]. The improved reconstruction performance was also demonstrated compared to static method.

In this paper, we carefully consider the *a priori* spatial and temporal correlations in EIT images. For spatial correlations, a novel exponential model is presented based on: 1) sensitivity weighting, 2) an exponentially model of inter-element correlations, and 3) a smoothness constraint for poor sensitivity regions. In order to avoid dependence on mesh element density, a closed form approximation to the integral is developed. The spatial prior model developed in this paper models the spatial variation in conductivity as a random walk process. It has the advantage over simpler prior models (such as the discrete Laplacian and NOSER priors) of accounting for the spatial interactions in a way that is independent of element size. However, linear prior models cannot account for sharp edges and piecewise constant conductivity regions; it is possible to use total variation priors for this case [22], at the expense of significantly longer iterative solutions. For the temporal correlations, an exponential model is presented of inter-frame correlations (based on an exponential constraints γ), and an automatic approach to determine γ from the measurements is developed. The choice of temporal window d depends on several considerations; large d may decrease artefacts and reconstruction noise; however, it increases the size of the matrix inverse, and increases the condition number of the matrix to be inverted. In order to implement a temporal solver in an EIT system for real-time imaging, a delay

must be introduced between the measurements and reconstruction to allow acquisition of d "future frames". This corresponds to the linear phase filters used in digital signal processing applications. For fast EIT systems, with frame rates above 15 frames/sec, a choice of $d = 3$ introduces a delay of 200 ms. One core assumption of linearized time difference imaging is that conductivity variation is small. This allows the solution to assume that $\mathbf{J}$ does not vary during the $2d + 1$ frames considered in the reconstruction formulation. In the (relatively unlikely) case that $\mathbf{J}$ could not be assumed constant, the choice of d would need to be limited by the rate of change of background conductivity.

Comparisons of reconstructed images with these algorithms show that increasing consideration of prior correlations does improve the reconstructed image quality. In figures. 3, 4, we compare four approaches: traditional one-step GN, GN with temporal prior, GN with 3-D spatial prior and GN with 4-D prior. These results indicate that the temporal prior provides better image SNR and resolution compared with the tradition GN method. The 3-D spatial prior shows still better resolution; however, the 3-D spatial prior is more sensitive to noise than temporal prior. The 4-D prior shows a combined advantage advantage with less noise sensitivity. Some interesting effects are that the GN and temporal reconstructions show more disjoint image elements, which would appear to be due to a lack of smoothness constraint. Another effect is a circumferential elongation of the reconstructed object in the direction of movement in the temporal and 4-D reconstructions. This is a consequence of the temporal model accounting for additional data from times before and after the current instant.

In this paper, the ventricular ejection blood flow is simulated as a conductive sphere which moves laterally and upward in a helical pattern. This is a simplification which matches the velocity, direction and ejection volume during systolic ejection; however, the phyiological blood transport is much more complicated, which we do not simulate.

In summary, this paper proposes a four dimensional regularization for EIT reconstruction algorithms. We demonstrate that it is advantageous to take into account any spatial and temporal correlations which exist in the underlying images. We recommend the temporal method for cases in which the data noise is high and the underlying conductivity changes are rapid with respect to the frame rate. If the frame rate is much larger than the conductivity changes, then time averaging of measurements will provide the same effect with a simpler algorithm. Similarly, if data noise is very low, it does not help to

consider measurements from data frames at different times. However, we propose that the consideration of temporal and spatial correlations will generally be advantageous for EIT image reconstruction, and, most likely, for other imaging modalities as well.

Acknowledgements This work was supported by a grant from NSERC Canada.

References

1. Adler A., Guardo R., Electrical impedance tomography: regularised imaging and contrast detection, *IEEE Trans. Medical Imaging*, vol. 15, pp. 170-179 (1996)
2. Adler A., Guardo R., Berthiaume Y., Impedance imaging of lung ventilation: Do we need to account for chest expansion? *IEEE Trans. Biomed. Eng.*, vol. 43(4), pp.414-420 (1996)
3. Adler A., Lionheart W.R.B., Uses and abuses of EIDORS: An extensible software base for EIT, *Physiol. Meas*, vol. 27, pp. 25-42 (2006)
4. Adler A., Dai T., Lionheart W.R.B., Temporal image reconstruction in electrical impedance tomography, *Physiol. Meas.*, vol. 28, pp. 1-11 (2007)
5. Babaeizadeh S. and Brooks D.H., Effects of electrode location error on boundary element impedance tomography solutions: CR bounds and simulation results, *3rd IEEE ISBI: Nano to Macro*, pp. 1080-1083 (2006)
6. Babaeizadeh S. and Brooks D.H., Electrical impedance tomography for piecewise constant domains using boundary element shape-based inverse solutions, *IEEE Trans. on Medical Imaging*, vol. 26, No. 5, pp. 637-647 (2007)
7. Bacrie C.C., Goussard Y., Guardo R., Regularized reconstruction in electrical impedance tomography using a variance uniformization constraint, *IEEE Trans.Med.Imag.,* vol. 16(5), pp. 562-571 (1997)
8. Bollmann A., Kanuru N.K., McTeague K.K., Walter P.F., DeLurgio D.B., Langberg J.J., Frequency analysis of human atrial fibrillation using the surface electrocardiogram and its response to ibutilide, *Am J Cardiol.*, vol. 81(12), pp. 1439-1445 (1998)
9. Boone K.G., Holder D.S., Effect of skin impedance on image quality and variability in electrical impedance tomography: a model study. *Med. Biol. Eng. Comput.*, vol. 34(5), pp. 351-354 (1996)
10. Cheney M., Isaacson D., Newell J.C., Simske S., Goble J.C., NOSER: an algorithm for solving the inverse conductivity problem, *Int.J.Imaging Syst.Technol.*, vol. 2, pp. 66-75 (1990)
11. Colton D., Kress R., *Inverse Acoustic and Electromagnetic Scattering Theory*, Springer, Berlin, (1992), p. 121, 289 (new edition: 1998, p. 133, 304)
12. Dai T., Soleimani M., Adler A., Four-Dimensional Regularization for Electrical Impedance Tomography Imaging, in *VIII Conf Electrical Impedance Tomography,* Graz, Austria, Aug 29 Sept 2 (2007)

13. Dehgani H., Soni N., Halter R., Hartov A., Paulsen K.D., Excitation patterns in three-dimensional electrical impedance tomography, *Physiol. Meas.*, vol. 26, pp. 185-197 (2005)
14. Eyuboglu B.M., Brown B.H., Barber D.C., In vivo imaging of cardiac related impedance changes, *IEEE Eng. Med. Biol. Mag.*, vol. 8(1), pp. 39-45 (1989)
15. Frerichs I., Electrical impedance tomography (EIT) in applications related to lung and ventilation: a review of experimental and clinical activities, *Physiol. Meas.*, vol. 21, pp. 1-21 (2000)
16. Van Genderingen H.R., van Vught A.J., Jansen J.R.C., Regional lung volume during high-frequency oscillatory ventilation by electrical impedance tomography, *Crit. Care Med.*, vol. 32, pp, 787-794 (2004)
17. Graham B., Adler A., Electrode Placement Configurations for 3D EIT, *Physiol. Meas.*, vol. 28, pp, 29-44 (2007)
18. Hammermeister K.E., Brooks R.C., Warbasse J.R., The rate of change of left ventricular volume in Man: I. Validation and peak systolic ejection rate in health and disease, *Circulation*, vol. 49, pp. 729-738 (1974)
19. Harris N.D., Brown B.H., Barber D.C., Continuous monitoring of lung ventilation with electrical impedance tomography, *Med. Biol. Soc.*, pp. 1754-1755 (1992)
20. Holder D.S., Electrical impedance tomography of brain function, *Brain Topography*, vol. 5, pp. 87-93 (1992)
21. Kohler B.U., Henning C., Orglmeister R., The principles of software QRS detection, *IEEE Eng Med Biol Mag.*, vol. 21, pp. 42-57 (2002)
22. Lionheart W., Polydorides N., Borsic A., Chap1.1: Why is EIT so hard, in *Electrical impedance tomography: methods, history and applications*, Holder D S, Ed. Bristol and Philadelphia, IOP, (2005)
23. Metherall P., Barber D.C., Smallwood R.H., Brown B.H., Three dimensional electrical impedance tomography, *Nature*, vol. 380, pp. 509-512 (1996)
24. Ormiston J.A., Shah P.M., Tei C., Wong M., Size and motion of the mitral valve annulus in man. I. A two-dimensional echocardiographic method and findings in normal subjects, *Circulation*, vol. 64, pp. 113-120 (1981)
25. Schmitt U., Louis A.K., Efficient algorithms for the regularization of dynamic inverse problems: I. Theory, *Inverse Problems*, vol. 18(3), pp. 645-658 (2002)
26. Schmitt U., Louis A.K., Wolters C., Vauhkonen M., Efficient algorithms for the regularization of dynamic inverse problems: II. Applications, *Inverse Problems*, vol. 18(3),pp. 659-676 (2002)
27. Seppanen A., Vauhkonen M., Vauhkonen P.J., Somersalo E., Kaipio J.P., State estimation with fluid dynamical models in process tomography-an application with impedance tomography, *Inverse Problems*, vol. 17, pp. 467-483 (2001)
28. Soleimani M., Adler A., Dai T., Peyton A.J., Application of a single step temporal imaging of magnetic induction tomography for metal flow visualization, *Insight*, vol. 50(1), pp. 25-29 (2008)
29. Tidswell A.T., Gibson A., Bayford R.H., Holder D.S., Electrical impedance tomography of human brain activity with a two-dimensional ring of scalp electrodes, *Physiol. Meas.*, vol. 22, pp. 167-175 (2001)

30. Tossavainen O.P., Vauhkonen M., Heikkinen L.M., Savolainen T., Estimating shapes and freesurfaces with electrical impedance tomography, *Measurem. Sci. Technol.*, vol. 15, pp. 1402-1411 (2004)

31. Wilkinson A.J., Randall E.W., Cilliers J.J., Durrett D.R., Naidoo T., Long T., A 1000-measurement frames/second ERT data capture system with real-time visualization, *IEEE Sensors Journal.*, vol. 5, pp 300-307 (2005)

32. Wolf G.K., Arnold J.H., Noninvasive assessment of lung volume: respiratory inductance plethysmography and electrical impedance tomography, *Crit. Care Med.*, vol. 33, pp. 163-169 (2005)

33. Vauhkonen P.J., Vauhkonen M., Savolainen T., Kaipio J.P., Three-dimensional electrical impedance tomography based on the complete electrode model, *IEEE Trans, Biomedical Engineering*, vol. 46, no. 9, pp. 1150-1160 (1999)

34. Vauhkonen M., Karjalainen P.A., Kaipio J.P., A Kalman filter approach to track fast impedance changes in electrical impedance tomography, *IEEE Trans. Biomed. Eng*, vol. 45, pp. 486-493 (1998)

35. Vonk-Noordegraaf A., Janse A., Marcus J.T., Bronzwaer J.G., Postmus P.E., Faes T.J.C., de Vries P.M., Determination of stroke volume by means of electrical impedance tomography, *Physiol. Meas.*, vol. 21, pp. 285-293 (2000)

36. Yorkey T.J., Webster J.G., Tompkins W.J., Comparing reconstruction algorithms for electrical impedance tomography, *IEEE Trans. Biomed. Eng*, vol. 34, pp. 843-852 (1987)